

Effect of particle size on the phase transformation behavior and equation of state of Si under hydrostatic loading

Sorb Yesudhas^{1*}, Valery I. Levitas^{1,2,3*}, Feng Lin¹, K. K. Pandey⁴, and Maddury Somayazulu⁵

¹Department of Aerospace Engineering, Iowa State University, Ames, Iowa 50011, USA

²Department of Mechanical Engineering, Iowa State University, Ames, Iowa 50011, USA

³Ames National Laboratory, Iowa State University, Ames, Iowa 50011, USA

⁴High Pressure & Synchrotron Radiation Physics Division, Bhabha Atomic Research Centre, Mumbai 400085, India

⁵HPCAT, X-ray Science Division, Argonne National Laboratory, Argonne, Illinois 60439, USA

*Corresponding authors. Email: sorbya@iastate.edu, vlevitas@iastate.edu

High-pressure synchrotron X-ray diffraction (XRD) studies have been conducted on three types of Si particles (micron, 100 nm, and 30 nm). The pressure for initiation of Si-I→Si-II phase transformation (PT) essentially increases with a reduction in particle size. For 30 nm Si particles, Si-I directly transforms to Si-XI by skipping the intermediate Si-II phase, which appears during the pressure release. The evolution of phase fractions of Si particles under hydrostatic compression is studied. The equation of state (EOS) of Si-I, Si-II, Si-V, and Si-XI for all three particle sizes is determined, and the results are compared with other studies. A simple iterative procedure is suggested to extract the EOS of Si-XI and Si-II from the data for a mixture of two and three phases with different pressures in each phase. Using previous atomistic simulations, EOS for Si-II is extended to ambient pressure, which is important for plastic strain-induced phase transformations. Surprisingly, the EOS of micron and 30 nm Si are identical, but different from 100 nm particles. In particular, the Si-I phase of 100 nm Si is less compressible than that of micron and 30 nm Si. The reverse Si-V→Si-I PT is observed for the first time after complete pressure release to the ambient for 100 nm particles.

I. Introduction

Silicon is the second most abundant element on the Earth's crust after oxygen. The

outstanding electronic properties of this covalent semiconductor ($E_g = 1.1$ eV) find applications in information technology, photovoltaics, nano-electromechanical systems (MEMS/NEMS), etc¹⁻⁵. Si has been considered a promising platform with tremendous potential for advancing scaled-up quantum computing⁵. Recent studies reveal that Si-III is a direct ultra-narrow band gap semiconductor with a band gap of 30 meV, which can be used in infrared plasmonic devices⁶. Silicon undergoes multiple polymorphic phase transformations under high pressure⁷⁻¹². The scaling down of Si from a micron to nm size shows extraordinary electronic, optical, and mechanical properties¹³⁻¹⁶.

With hydrostatic compression, the ambient cubic diamond Si-I phase (S.G: $Fd\bar{3}m$, $Z=8$) undergoes a pressure-driven cubic to tetragonal Si-II (S.G: $I41/amd$, $Z = 4$) reconstructive type phase transformation (PT) at around 11 GPa as a result of stretching of Si-1 unit cell along $[100]$, $[010]$ and compression along $[001]$ ⁷⁻¹² with a significant volume collapse of 23.7%. This PT is accompanied by a semiconductor-to-metal transition⁷⁻¹². With further compression, the antiparallel displacements of atoms in the Si-II lattice along the crystallographic c -axis by ± 0.068 induce the distortion of the tetragonal Si lattice to another lower symmetry orthorhombic Si-XI (S.G: $Imma$, $Z=4$) lattice^{7,11}. This transition involves no coordination number change but is coupled with the Wyckoff position change from $4(a)$ to $4(e)$ ^{7,11}. Similarly, the antiparallel displacements of Si atoms in the orthorhombic lattice along the c -axis by $\pm 0.057c$ bring about orthorhombic to another displacive type simple hexagonal phase Si-V (S.G: $P6/mmm$, $Z=1$)⁷. The coordination number of Si-I, Si-II, Si-XI, and Si-V phases are 4, 6, 6, and 8, respectively. Si exhibits quite different structural behavior during unloading. With fast unloading from Si-II, two tetragonal phases are obtained: Si-VIII (S.G: $P41212$) and Si-IX (S.G: $P422$)¹⁷. When Si-II is unloaded slowly using a liquid pressure transmitting medium, a rhombohedral semiconducting phase Si-XII (S.G: $R\bar{3}$), is observed at 9.9 GPa, which coexists with the Si-III (S.G: $Ia\bar{3}$) (Si-XII+Si-III) below 3.2 GPa, and is in turn almost transform to Si-III at 2 GPa¹⁸⁻¹⁹. A small portion of Si-XII was noticed even after the complete pressure release¹⁸⁻¹⁹.

When a material is compressed in a DAC or compressed and sheared in a rotational DAC without a pressure-transmitting medium, the material undergoes plastic strain-induced PTs, which show different behavior in comparison with the PTs observed under hydrostatic conditions²⁰⁻²³. The initiation of phase transformation pressure for samples subjected to quasi-hydrostatic

compression is determined by the preexisting defects, like dislocations and grain boundaries. In contrast, the creation of new defects during the plastic flow with much stronger stress concentrators, like dislocation pileups with a large number of dislocations, is responsible for a significant reduction in PT pressure for plastic strain-induced phase transformation²¹⁻²³. The determination of pressure in plastic strain-induced PTs study requires an EOS for each phase of the material, which is determined under hydrostatic conditions. The actual (average) pressure at a radial point (r) on the sample will be the sum of the product of the pressure in each phase multiplied by corresponding volume fractions. The radial pressure distribution in a sample compressed in a DAC or compressed and sheared in a rotational DAC is very heterogeneous^{20,24-27}. It is determined using the measured radial distribution of the volume of phases and applying EOS of these phases determined under hydrostatic conditions. In particular, silicon exhibits quite complex PT sequence along the sample diameter under non-hydrostatic compression and torsion, and calculating pressure in the Si phases at multiple points along the sample diameter for various pressures requires accurate EOS of different Si phases with P - V data from the pure Si phases²⁰. With plastic compression and shear, we reported a drastic pressure reduction of Si-I \rightarrow Si-II PT from 13.5 GPa to 2.6 GPa for micron Si, and it is from 16.2 GPa to 0.3 GPa for 100 nm Si²⁰. Thus, EOS for Si II (and other phases) should be robustly extrapolated for pressures outside the region of the existence of phases under hydrostatic loading. The only way to do this is to utilize theoretical (first principle) results, which we will utilize in the current paper.

Despite several high-pressure PT studies reported for various grain sizes of silicon^{10, 13-15, 28-29}, a detailed comparative high-pressure structural behavior of different grain sizes of Si is missing. Using Le Bail fitting of synchrotron XRD data, the equation of state of micron size Si up to one megabar pressure has been determined recently²⁸. In addition, the phase transition behavior of silicon with different morphology and size has been investigated²⁹. However, this study did not provide a detailed XRD analysis to extract the lattice parameters, volume of high-pressure phases, and phase fractions, which are crucial to understanding the quantitative evolution of high-pressure phases³⁰. Also, we are not aware of any high-pressure studies that reported phase fractions of high-pressure phases of Si, and most of the studies utilized Le Bail fitting on XRD data, which led to inaccuracy in the determination of lattice parameters and, hence, the volume of high-pressure phases. The preferred orientation effects on high-pressure phases of Si pose difficulties in extracting phase fractions. Also, the experimental EOS of Si-II is not available in the literature

because of the narrow pressure range of its existence, and it always coexists with other phases. Without knowing the volume fraction of each phase, it is impossible to extract the pressure and EOS of each phase in the mixture.

In this work, we performed a first detailed comparative study of the structural behavior of silicon with three different particle sizes, 1 μm , 100 nm, and 30 nm, under hydrostatic compression with high-pressure synchrotron X-ray diffraction technique. The volume and phase fraction of Si phases are extracted using the Rietveld refinement method. A known theoretical EOS for Si-II is used. In such a way, the EOS of different Si phases with different particle sizes were studied and compared with other reports, if available.

II. Experimental Details

Single crystal, 100 nm, and 30 nm Si particles were used for the high-pressure studies. The single crystal silicon sample was purchased from Sigma-Aldrich (CAS NO.: 7440-21-3) and was powdered to a ~ 1 μm fine powder by grinding with a pestle and mortar. The Si nano samples with a particle size of < 100 nm (TEM) and purity of ≥ 98 % were purchased from Sigma-Aldrich (CAS No.: 7440-21-3). The Si nanopowders with a particle size of 30 nm were purchased from Meliorum Technologies, Inc. High-pressure experiments were carried out using symmetric type diamond anvil cells (DACs) and SSDAC (from DAC Tools, LLC) with culet diameters of 300 and 400 μm . The micron and 100 nm samples were compacted by pressing the samples between two stainless steel (S. S.) gaskets. A small pellet of the compacted sample was placed into the S. S. sample chamber. The 30 nm Si nanopowder was slightly pressed using a hydraulic press to make a thin pellet. The He PTM was used to achieve hydrostatic conditions³¹. The pressure in the PTM and sample was determined by the ruby fluorescence method³². All the high-pressure synchrotron XRD experiments were carried out at the 16-ID-B beam line, HPCAT, utilizing Advanced Photon Source with X-ray wavelengths, 0.4246 \AA and 0.3445 \AA and the X-ray beam with a spot size of 5 μm x 4 μm . The 2D XRD image was converted to a 1D pattern using diopbase software³³. The XRD patterns were refined using GSAS-II software to extract the lattice parameters and volume fractions of Si phases using the Rietveld refinement method³⁴. The spherical harmonics texture model was used to fit the high-pressure Si phases. The bulk modulus and its first derivative were calculated using the EOSFIT-7 GUI program³⁵.

III. Results and Discussions

III.1. Phase transformation behavior

High-pressure XRD patterns of micron size Si for representative pressures and the pressure dependence of the volume/ Z are shown in Figs. 1a, b. The Si-I phase is stable up to ~ 13.3 GPa, and at ~ 13.5 GPa, it undergoes a pressure-driven symmetry lowering structural phase transformation into a mixture of tetragonal Si-II and an orthorhombic Si-XI (Imma) phases (Figs. 1a, b). The XRD pattern at 13.5 GPa can be fitted with all these three phases (Si-I, Si-II, and Si-XI), suggesting the observed transition is a mixed-phase PT, and these phases coexist up to 14.1

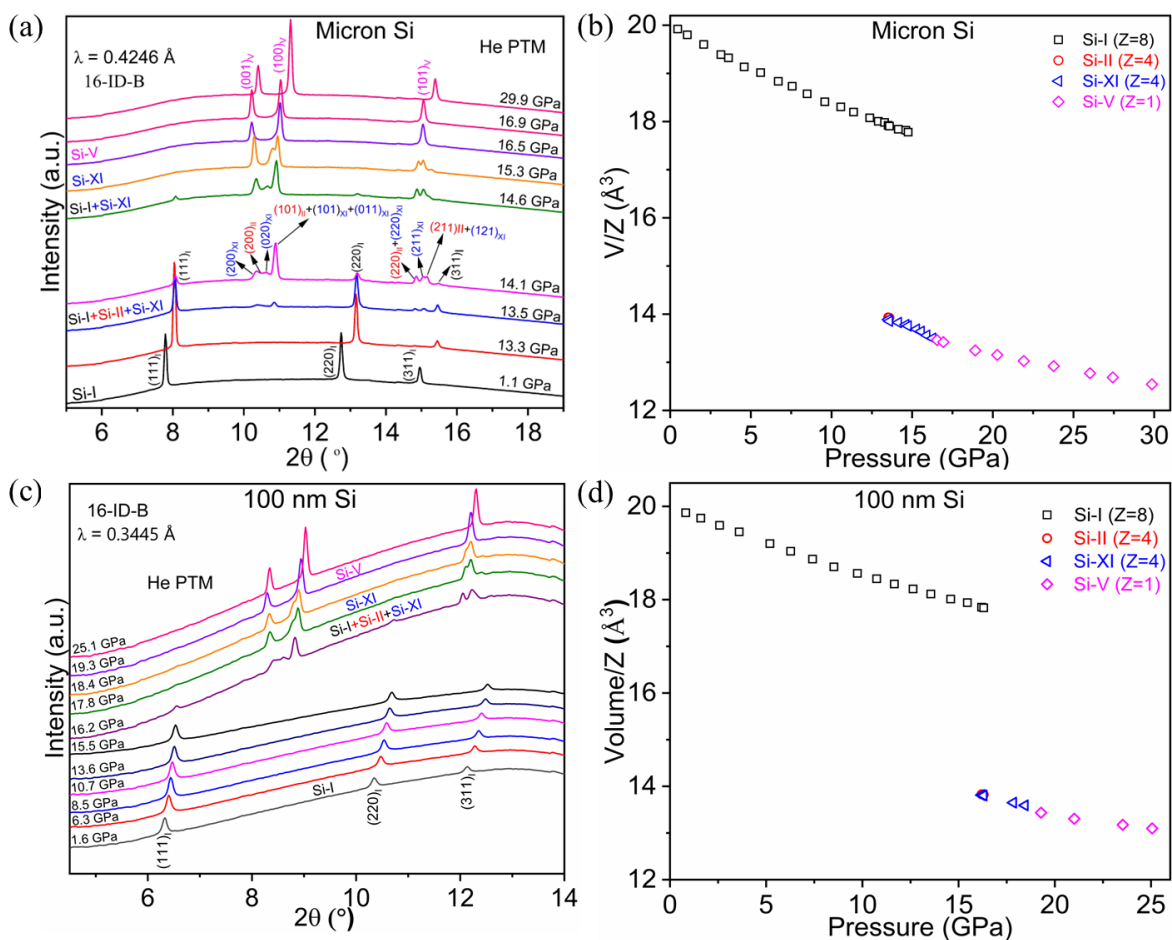


Fig. 1. Pressure-induced phase transformations in micron and 100 nm Si. (a) High-pressure XRD patterns of micron size Si at various pressures. The Si-I, Si-II, and Si-XI mixed phases are indexed at 14.1 GPa. The subscripts I, II, XI, and V of the (hkl) Bragg planes represent the Bragg planes of the Si-I, Si-II, Si-XI, and Si-V phases, respectively. **(b)** Volume/ Z vs. pressure for micron size Si. The error bar is excluded from all the figures if it overlaps with the symbols. **(c)** High-pressure XRD patterns of 100 nm Si for selected pressures. **(d)** Volume/ Z vs. pressure of 100 nm Si.

GPa (Figs. 1a, 1b). The enhancement of the intensity of the XRD peaks of the Si-II and Si-XI lattices and a dramatic drop in that of the Si-I phase evidence PT of the Si-I lattice into Si-II and Si-XI lattices. At 14.6 GPa, a portion of Si-I and the remnant of the Si-II lattices transform into the Si-XI lattice, and the Si-I is seen to coexist with Si-XI (Figs. 1a, b). With further pressure increase, the remaining Si-I lattice transforms into Si-XI lattice at 15.3 GPa (Figs. 1a, b). At 16.5 GPa, a pure Si-V phase is formed, which is stable up to the maximum pressure achieved, 29.9 GPa. The Rietveld refinement of the Si-V phase for the micron Si at 23.8 GPa is shown in Fig. A1. The Si-I→Si-II PT is associated with a volume collapse of 22.3 %, whereas the Si-II→Si-XI and Si-XI→Si-V PTs are continuous (Figs.1a, b). Our results on micron Si agree with those obtained in²⁸. The observed onset of Si-I→Si-I+Si-II+Si-XI PT at 13.5 GPa agrees with the initiation of PT in²⁸. When the pressure in the sample is completely released to the ambient, a coexistence of Si-III and Si-XII phases is discerned.

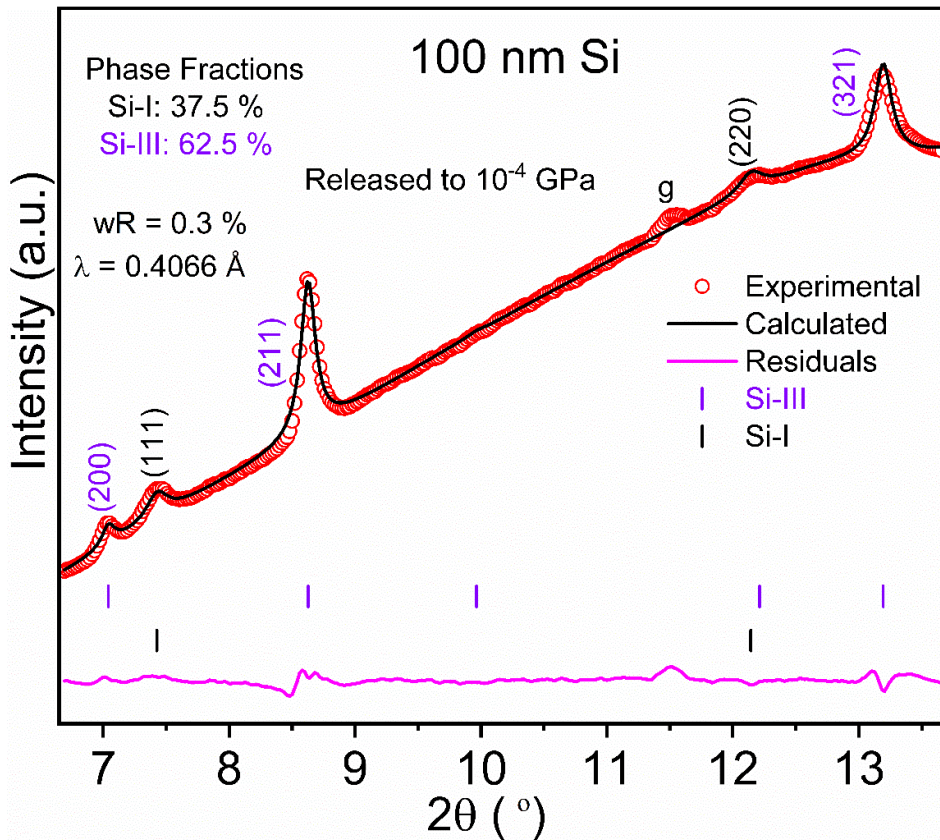


Fig. 2. The first observation of reverse Si-V→Si-I PT in hydrostatic high-pressure experiments. Rietveld refinement of 100 nm Si after releasing to the ambient from Si-V at 25.1 GPa. Si-I phase is coexisting with Si-III. ‘g’ is the gasket peak.

Fig. 1c shows the high-pressure XRD pattern of 100 nm Si for selected pressures. The PT sequence in 100 nm Si is similar to that in micron Si, except for the initiation of PT pressures of high-pressure phases. As the particle size is reduced from micron to 100 nm Si, the Si-I transformed into a mixture of Si-I, Si-II, and Si-XI at 16.2 GPa, which is 2.7 GPa higher as compared to the initiation of PT pressure obtained in micron Si (Figs. 1c, d and Fig. A2). The Si-I, Si-II, and Si-XI phases are seen to coexist in a very narrow pressure range. At 17.8 GPa, the Si-I and Si-II lattices completely transform into Si-XI (Figs. 1c, d). The Si-XI→Si-V PT completes at 19.3 GPa, stable up to the maximum pressure of 25.1 GPa achieved in the experiment (Figs. 1c, d). When the pressure is completely released to the ambient, Si-I (37.5 %) and Si-III (62.5 %) phase mixtures are obtained (Fig. 2). The reverse Si-V→Si-I PT is observed for the first time in the hydrostatic compression-decompression experiments (Fig. 2).

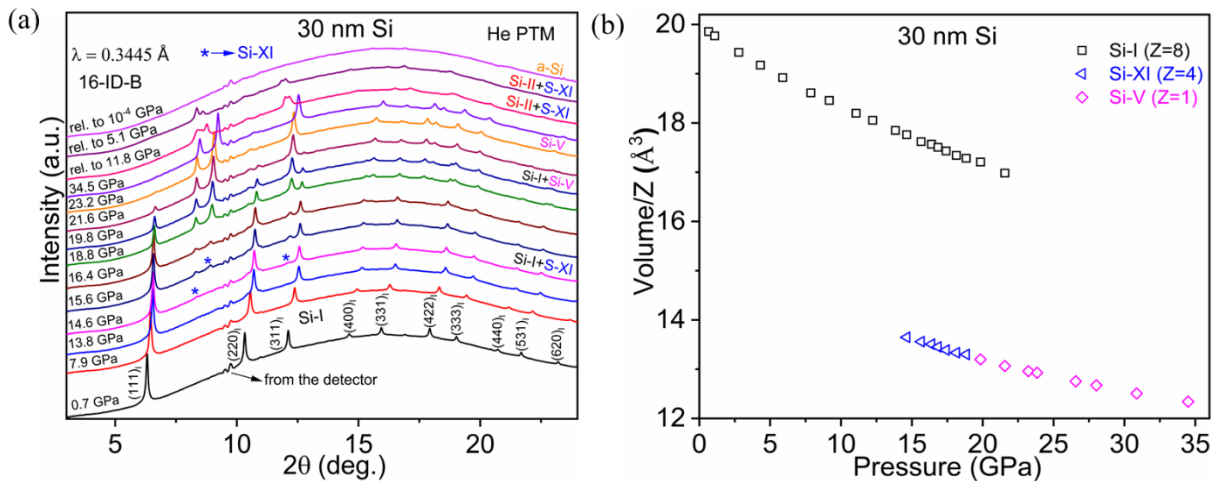


Fig. 3. Pressure-induced phase transformation in 30 nm Si. (a) High-pressure XRD patterns of 30 nm Si at various pressures. **(b)** Volume/ Z vs. pressure of 30 nm Si.

In contrast to micron and 100 nm Si particles, the 30 nm Si particles start directly transforming into a Si-XI phase at 14.6 GPa by skipping the intermediate Si-II phase (Figs. 3a, b). The XRD patterns up to 18.8 GPa can be fitted well with Si-I and Si-XI phase coexistence (Si-I+Si-XI). The XRD pattern at 18.8 can be fitted to both Si-I+Si-XI and Si-I+Si-V phase coexistences, but we obtained the best fit with Si-I+Si-XI phase mixture. At 19.8 GPa, the Si-V phase appears, which coexists with Si-I. The Si-I phase coexists with Si-V up to 23.2 GPa. Note that perfect Si-I crystal shows transverse acoustic phonon instability at 18.3 GPa, according to the first principle simulations³⁶, i.e., it cannot exist above this pressure. Thus, Si-I is stabilized by size and surface effects. After pressure release to ambient, amorphous Si is observed, like in^{29,38}. The

Si-I→Si-XI PT is accompanied by a volume collapse of 23.2 %, whereas the Si-XI→Si-V PT is practically continuous. For micron and 100 nm Si, the Si-II and Si-XI phases coexist over a very narrow pressure range of < 1 GPa. For 30 nm Si, the Si-I coexists with Si-XI (Si-I+Si-XI) and Si-V (Si-I+Si-V) over an extensive pressure range of about 7 GPa (Fig. 3).

The initiation pressure for the Si-I→Si-II/Si-XI PT increases from 13.5 GPa to 16.2 GPa for 100 nm Si and is 14.6 GPa for 30 nm Si (Figs. 1c, d, and 2). A pure Si-XI phase is observed for micron and 100 nm Si at 15.3 GPa and 18.1 GPa, respectively, whereas the Si-I phase always coexists with the Si-XI phase for 30 nm Si (Figs. 1 and 2). The initiation pressure for Si-XI→Si-V

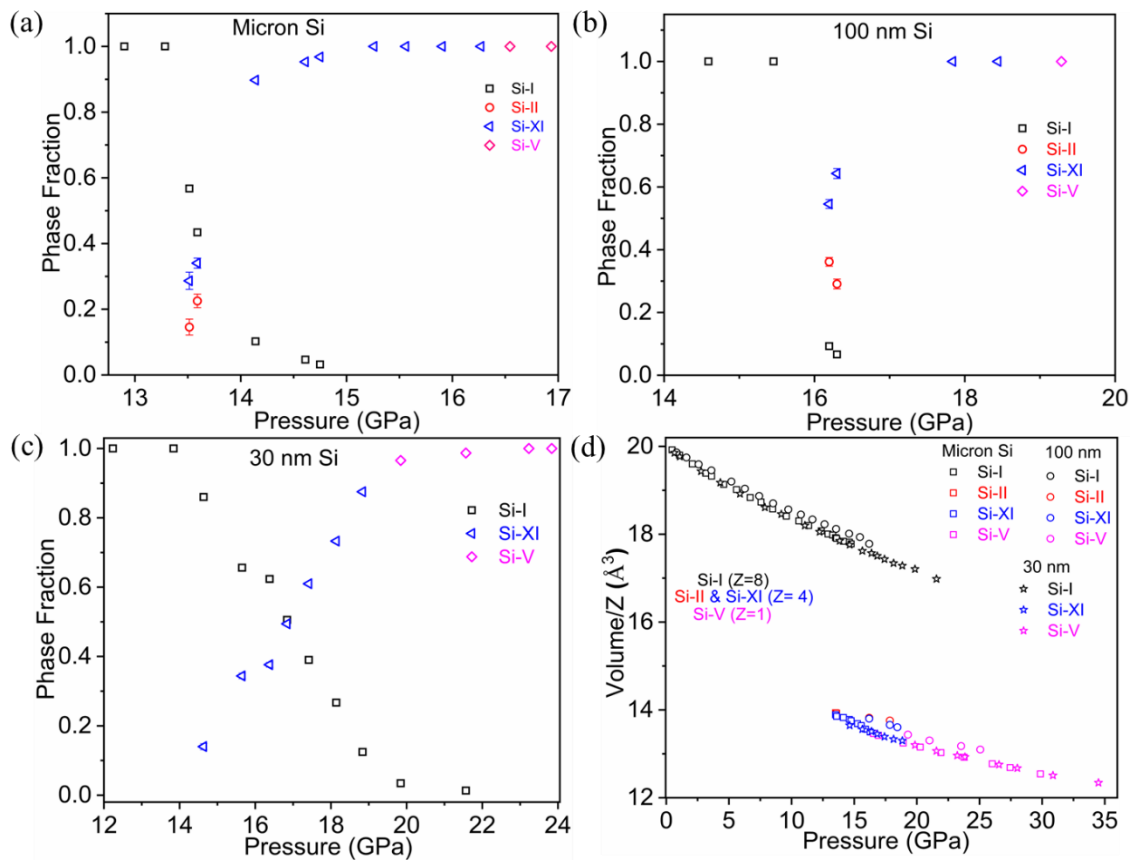


Fig. 4. Evolution of phase fraction and volume of Si phases under pressure. (a) Phase fraction vs. pressure of micron Si. **(b)** Phase fraction vs. pressure of 100 nm Si. **(c)** Phase fraction vs. pressure of 30 nm Si, and **(d)** a comparison of volume/Z of Si particles vs. pressure.

increases from micron to 30 nm Si (16.5 GPa for micron Si, 19.3 GPa for 100 nm Si, and 19.8 GPa for 30 nm Si). The elevation of Si-I→Si-II PT pressure upon reducing the particle size is due to the reduction in the number of stress concentrators (dislocations and grain boundary effects) and

contribution from the surface energy. The surface energy strongly increases during Si-I→Si-II PT, suppressing this PT for all particles. This effect increases with a reduction in particle size, and for 30 nm Si, Si-XI and V appear before Si-II due to their smaller surface energy.

These results raise theoretical challenges for their quantitative descriptions. Xuan *et al.*²⁹ claimed that the compression of Si nanoparticles with and without a pressure-transmitting medium will not alter the phase-transition sequence. However, in our high-pressure studies on 30 nm Si particles, the non-hydrostatic compression alters the phase transformation sequence and drastically reduces the onset of Si-I→Si-II PT pressure²⁰. With He PTM, Si-I directly transforms to Si-XI by skipping Si-II, whereas we observed Si-II at 4.9 GPa for 30 nm Si under non-hydrostatic compression²⁰.

The phase fraction and volume versus pressure for all three types of Si particles are shown in Figs. 4a-d. For micron Si, the maximum phase fraction of Si-II observed is 23 % at 13.6 GPa, whereas it is 36 % at 16.2 GPa for 100 nm Si. The coexistence range of the Si-II phase with Si-I and Si-XI is very narrow for micron and 100 nm Si particles, and Si-II does not appear for 30 nm Si. The V/Z of Si-I, Si-XI, and Si-V phases of micron and 30 nm Si exhibit an identical behavior (Fig. 4d). The phase fractions of Si-I and Si-XI phases in 30 nm Si particles at 14.6 GPa are 14 % and 86 %, respectively. Similarly, the phase fractions of Si-I and S-V at 19.8 GPa are 3.4 % and 96.6 %, respectively. During pressure release, Si-V transforms to a phase mixture of Si-II and Si-XI, which is stable down to 5.1 GPa. When the pressure is completely released to the ambient, it transforms to the amorphous phase, which agrees with^{29,38}.

III.2. Equation of state of Si phases

A. EOS for Si-I and Si-V

The volume at $P = 0$ (V_0), bulk modulus (B_0), and its first derivative (B'_0) of Si phases of micron, 100 nm, and 30 nm Si are calculated by fitting P - V data of corresponding phases to the Murnaghan, Birch-Murnaghan, and Vinet EOS³⁹⁻⁴⁰ (Figs. 5, 6), and the results are shown in Table 1. The bulk moduli values of the present work are compared with the most recent study in²⁸ (Table 1). Our B_0 and B'_0 values of Si-I for micron Si agree with the values reported in other references^{9,28,41} (Table 1). Moreover, the B_0 and B'_0 values of the Si-I phase agree with the values obtained by the ultrasonic measurements ($B_0 = 97.88$ GPa and $B'_0 = 4.23$)⁴¹. The volume at zero

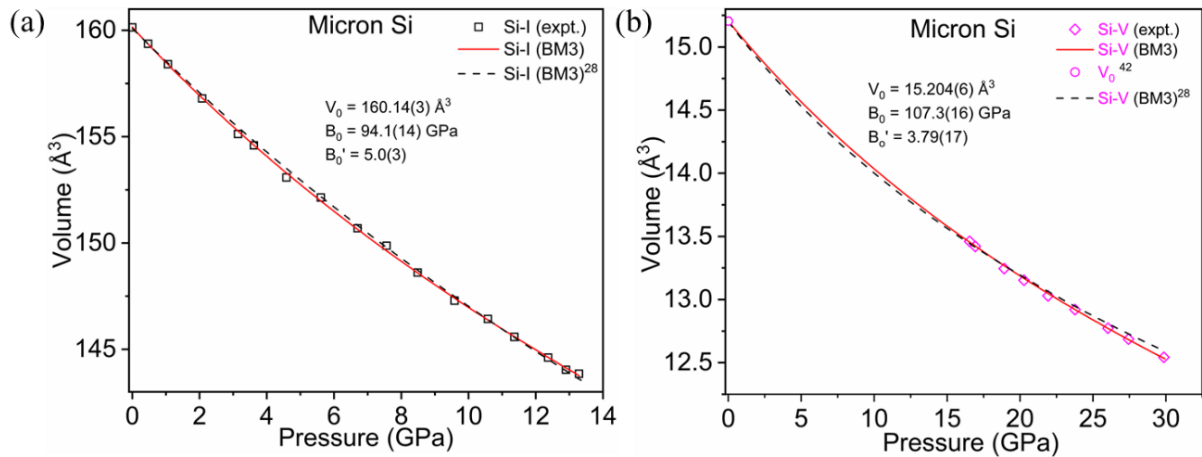


Fig. 5. Calculating bulk modulus and its derivative of **(a)** Si-I phase of micron Si. The dotted line represents the simulated EOS taken from²⁸. Volume vs. P of Si-I phase of micron Si. **(b)** Volume vs. P of Si-V phase of micron Si. V_0 is taken from⁴². The dotted line is the simulated pattern from²⁸.

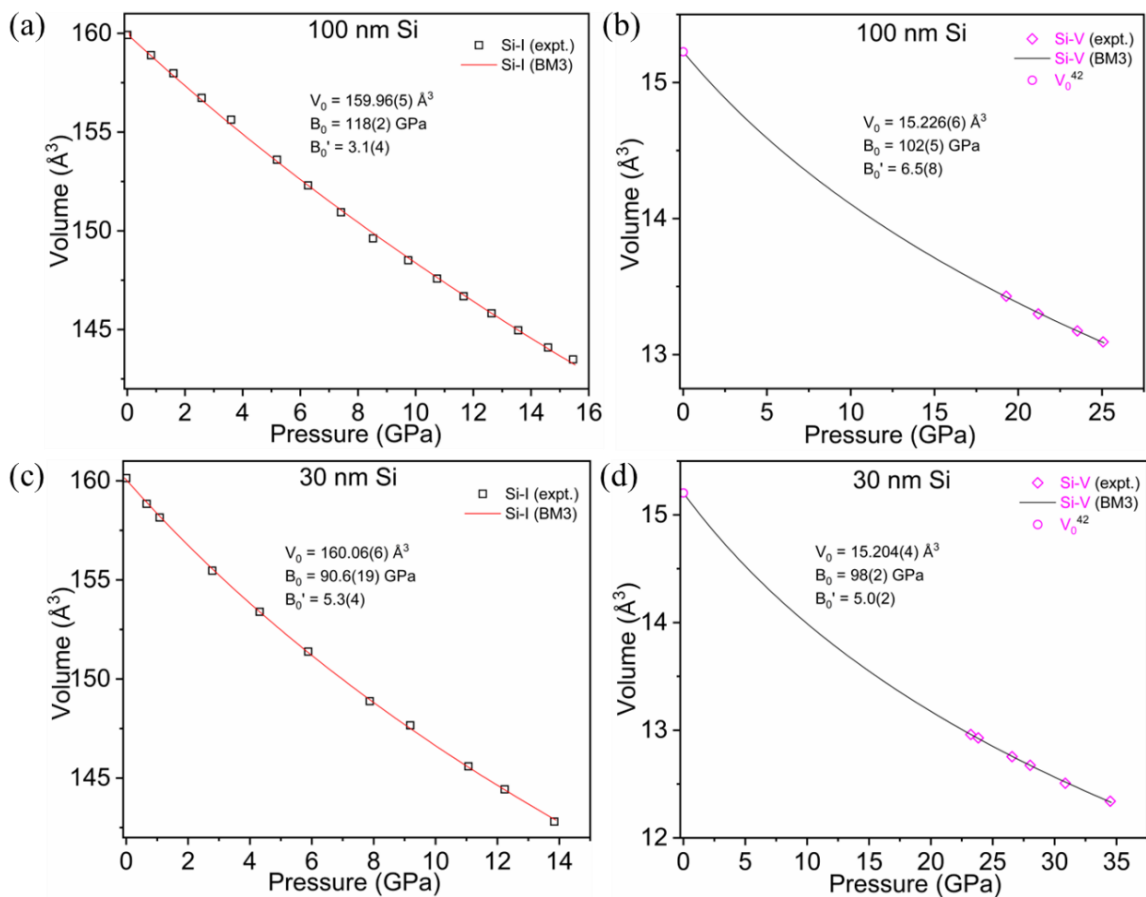


Fig. 6. EOS of **(a)** Si-I phase of 100 nm Si **(b)** Si-V phase of 100 nm Si. V_0 is taken from theory⁴². **(c)** Si-I phase of 30 nm Si **(d)** Si-V phase of 30 nm Si. V_0 is taken from theory⁴².

EOS		Micron Si		100 nm Si		30 nm Si	
		Si-I	Si-V	Si-I	Si-V	Si-I	Si-V
3 rd order	$V_0(\text{\AA}^3)$	160.14(3)	15.204(6)	159.96(5)	15.226(6)	160.06(6)	15.204(4)
Birch-	$B_0(\text{GPa})$	94.1(14)	107.3(16)	118(2)	102(5)	90.6(19)	98(2)
Murnaghan	B'_0	5.0(3)	3.79(17)	3.1(4)	6.5(8)	5.3(4)	5.0(2)
3 rd order	$V_0(\text{\AA}^3)$	160.088(8)	15.2(1)				
Birch-	$B_0(\text{GPa})$	101.5(3)	99(10)
Murnaghan ²⁸	B'_0	3.45(5)	5.0(6)				
2 nd order	$V_0(\text{\AA}^3)$	160.11(3)	15.206(6)	160.00(5)	15.225(13)	159.94(7)	15.203(9)
Birch-	$B_0(\text{GPa})$	98.5(5)	105.5(5)	113.5(8)	120.7(12)	96.9(8)	107.1(7)
Murnaghan	B'_0	4.0	4.0	4.0	4.0	4.0	4.0
	$V_0(\text{\AA}^3)$	160.14(3)	15.204(6)	159.96(5)	15.226(5)	160.05(6)	15.204(4)
Murnaghan	$B_0(\text{GPa})$	94.5(14)	108.6(16)	119(2)	105(4)	91.3(19)	100.0(18)
	B'_0	4.7(3)	3.47(16)	2.9(4)	5.6(5)	4.9(3)	4.44(17)
	$V_0(\text{\AA}^3)$	160.14(3)	15.204(6)	159.96(5)	15.226(6)	160.06(6)	15.204(4)
Vinet	$B_0(\text{GPa})$	93.9(14)	106.8(18)	119(2)	102(5)	90.4(19)	96(2)
	B'_0	5.1(3)	3.9(2)	3.1(4)	6.5(7)	5.4(4)	5.3(2)

Table 1. Volume at zero pressure $V_0(\text{\AA}^3)$, the bulk modulus $B_0(\text{GPa})$ and its first derivative (B'_0) of Si-I and Si-V phases of micron, 100 nm and 30 nm Si are calculated by fitting our experimental P - V data to the Murnaghan, second and third order Birch-Murnaghan, and Vinet EOS. The parameters of the third-order Birch-Murnaghan EOS from²⁸ are compared with the values obtained by our data.

pressure V_0 of the Si-V phase is taken from the theoretical prediction⁴² (15.204\AA^3). Figs. 5 and 6 demonstrate a good correspondence between analytical EOS and experimental data for EOS of Si-I and Si-V for all particles. The bulk moduli values of micron Si-V are slightly underestimated in²⁸ (Table 1), which is evident from the steepness of the P - V curve in Fig. 5b. Our values are more accurate because we used pure P - V data for Si-V, and we also calculated the volume using Rietveld refinement method. The Si-I phase of 100 nm Si is found to be less compressible when compared with micron and 30 nm Si (Fig. 4d, Table 1). The compressibility of ambient and high-pressure phases of 30 nm Si is comparable to the micron Si (Fig. 4d, Tables 1 and 2). In Fig 3d, the behavior of V/Z vs. P of micron Si is akin to the 30 nm Si; hence, all the equations of states of micron Si

can be used for 30 nm Si as well. Such a non-monotonous dependence of the EOS for Si-I on the particle size is unexpected and requires theoretical analysis. The EOS of Si-III was obtained in³⁷ (Table 2).

B. Extracting EOS for Si-II and Si-XI phases from phase mixtures

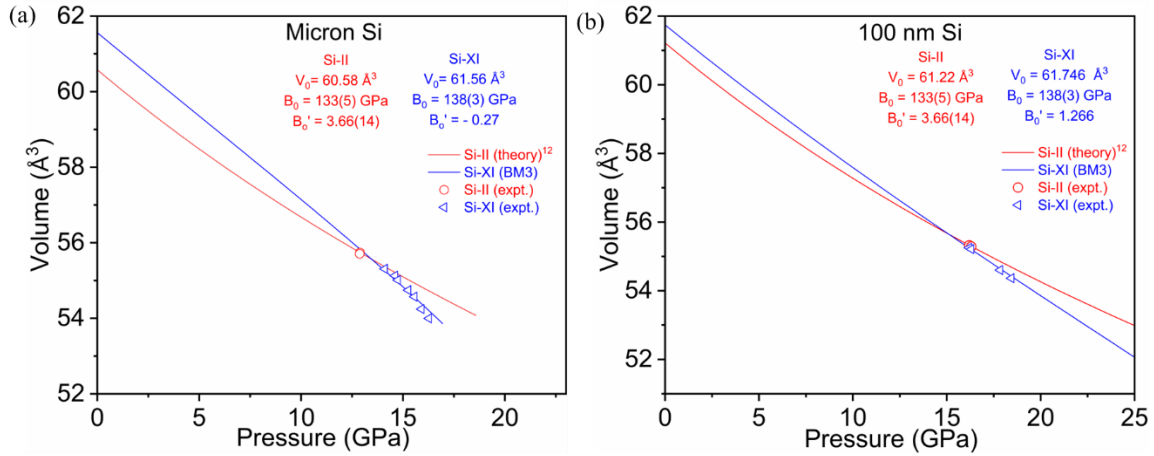


Fig. 7. EOS of Si-II and Si-XI phases of **(a)** pure micron Si and **(b)** 100 nm Si. The experimental data points for Si-II and Si-XI are shown in circles and triangles, respectively.

For micron Si XI, two experimental P - V data points of Si-XI coexist with Si-I and Si-II (Fig. 1); three data points coexist with Si-I; and there are four points for a single-phase Si-XI. For the coexisting of Si-I and Si-XI phases, as we know the pressure p_I and phase fraction c_I of pure micron Si-I (using pure Si-I EOS), the phase fraction c_{XI} of Si-XI, and the pressure P in the phase mixture measured by ruby. The pressure in pure Si-XI is obtained using the phase mixture rule,

$$P = c_I P_I + c_{XI} P_{XI} . \quad (1)$$

This gives us P - V data for three more points, total 7 points for pure Si-XI, in a broader pressure range, to fit BM3 EOS for Si-XI (Table 2 and Fig. 7). It is to be noted that, even under non-hydrostatic compression, Si-XI was not observed below 10 GPa for any particles, extrapolation below this value does not have practical importance²⁰. The same procedure was done for 100 nm Si particles. EOS for 30 nm Si-XI is the same as for micron particles.

Since we acquired only two data points for Si-II coexisting with Si-I and Si-XI for micron

and 100 nm Si, we used the theoretical P - V data from¹² for the Si-II EOS. First, using the phase mixture rule for a three-phase mixture

$$P = c_I P_I + c_{II} P_{II} + c_{XI} P_{XI} \quad (2)$$

with all known parameters but the pressure in Si-II P_{II} , we calculate P_{II} for two experimental points. P_{XI} is obtained by using Si-XI EOS (Fig. 8 and Table 2). According to¹², the Si-II is metastable at normal pressure, i.e., it can exist if retained instead of transforming to Si-XII and Si-III, which was confirmed experimentally for some sample points in²⁰. That is why interpolation down to zero pressure for Si-II is crucial.

The results are presented in Table 2. First, we determined EOS for Si-XI for micron and 100 nm Si based on our experimental data. Then, the theoretical data from¹² is described by the third order Birch Murnaghan EOS with $V_0 = 60.29$ (14) \AA^3 , $B_0 = 133$ (5) GPa and $B'_0 = 3.66$ (14) GPa.

EOS		Micron Si			100 nm Si	
		Si-II	Si-XI	Si-III	Si-II	Si-XI
3 rd order Birch-Murnaghan (This study)	V_0 (\AA^3)	60.58	61.56		61.22	61.746
	B_0 (GPa)	133(5)	138(3)	133(5)	138(3)
	B'_0	3.66(14)	-0.27		3.66(14)	1.266
3 rd order Birch-Murnaghan (Si-II ¹² , Si-XI ^{28,42} and our data)	V_0 (\AA^3)	60.29(14)	62.89(3)			
	B_0 (GPa)	133(5)	98(3)
	B'_0	3.66(14)	1.9(4)			
2 nd order Birch-Murnaghan (Si-III ³⁷)	V_0 (\AA^3)		68.52(24)			
	B_0 (GPa)	42(6)	292.36
	B'_0		4(1)	117.0 4.0		

Table 2. The BM3 EOS of Si-XI and Si-II phases of micron and 100 nm Si from our experimental P - V data with a mixture of two and three phases are obtained by using simple iterative procedure. The EOS for Si-II is also approximated by fitting simulated P - V data in¹² to the BM3 EOS. The EOS of Si-XI is also obtained by combining our data with data from²⁸ and one of the theoretical values for V_0 from⁴². EoS for Si-III is taken from³⁷

For micron particles, we combined our experimental points with theoretical data from¹², keeping the same $B_0 = 133(5)$ GPa and $B'_0 = 3.66(14)$ GPa, and obtained slightly higher $V_0 = 60.58$ Å³. A slightly higher V_0 than in¹² is reasonable because calculations in¹² are at 0 K and there is a thermal expansion while heating to room temperature.

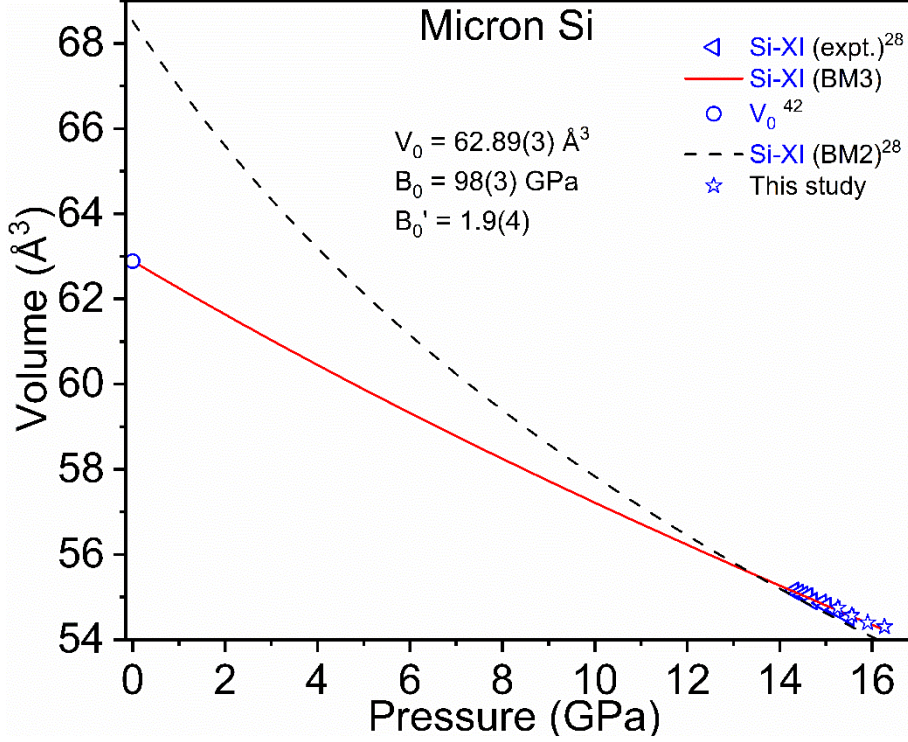


Fig. 8. Si-XI EOS of micron Si. The combined P - V data of pure Si-XI phase of micron Si from this work and also from²⁸ is fitted to the BM3 EOS with $V_0 = 62.89$ Å³, which is one of the theoretical values from⁴². Triangle and star symbols represent the pure Si-XI P - V data from²⁸ and from our work.

For 100 nm Si, two experimental points have slightly higher pressure (3.3 and 3.4 GPa) than for micron particles. That is why we keep the same B_0 and B'_0 , and slightly increase V_0 to 61.22(14) Å³. Then, we slightly refine V_0 and B'_0 for Si-XI to get approximately continuous P - V curve for Si-II to Si-XI transition at transition pressure (Fig. 7 and Table 2).

We have also calculated the EOS for micron Si-XI by combining our pure Si-XI P - V data with experiments from²⁸. We also utilized one of the theoretical values of $V_0 = 62.89(3)$ Å³ from⁴². The obtained EOS is compared in Fig. 8 with the BM2 EOS reported in²⁸ where a large value of

$V_0 = 68.52 \text{ \AA}^3$ was chosen¹². Moreover, in²⁸, the authors used both mixed and pure Si-XI P - V data to obtain BM2 EOS which is why the EOS from²⁸ shows a deviation from our Si-XI P - V data.

IV. Conclusions

A comparative study of high-pressure PT behavior of three types of Si viz, micron, 100 nm, and 30 nm Si is performed. The pressure for initiation of Si-I \rightarrow Si-II phase transformation (PT) essentially increases with a reduction in particle size. The Si-II and Si-XI phases of micron and 100 nm Si appear from Si-I simultaneously and coexist over a narrow pressure range of < 1 GPa, whereas for 30 nm Si, Si-I directly transforms to Si-XI (skipping Si-II), and Si-I coexists with Si-XI (Si-I+Si-XI) and Si-V (Si-I+Si-V) over a wide range of pressures. The increase in Si-I \rightarrow Si-II PT pressure with reduction in the particle size can be rationalized by the reduction in the number of stress concentrators (dislocations and grain boundary effects) and contribution from the surface energy. The surface energy strongly increases during Si-I \rightarrow Si-II PT, suppressing this PT for all particles. This effect increases with a reduction in particle size, and for 30 nm Si, Si-XI and V appear before Si-II due to their smaller surface energy. The evolution of phase fractions of Si particles under hydrostatic compression is presented for the first time. For 30 nm particles, Si-I coexists with Si-V up to 23.2 GPa. This is unexpected because the first principle simulations³⁶ produce transverse acoustic phonon instability at 18.3 GPa for perfect Si-I crystal, i.e., it cannot exist above this pressure. Consequently, Si-I is stabilized by size and surface effects. During full pressure release, the previously unreported reverse Si-V \rightarrow Si-I PT is observed. For 30 nm particles, complete unloading leads to Si-V \rightarrow amorphous Si PT. Obtained results find applications for the determination of pressure distribution in non-hydrostatic compression and shear of Si²⁰ and for developing quantitative models for PT evolutions as outlined in³⁰.

Acknowledgments: We thankfully acknowledge the support from NSF (CMMI-1943710 and DMR-2246991) and Iowa State University (Vance Coffman Faculty Chair Professorship and Murray Harpole Chair in Engineering). The high-pressure experiments were performed at HPCAT (Sector 16), Advanced Photon Source (APS), and Argonne National Laboratory. HPCAT operations are supported by DOE-NNSA's Office of Experimental Science. The Advanced Photon Source is a U.S. Department of Energy (DOE) Office of Science User Facility operated for the DOE Office of Science by Argonne National Laboratory under Contract No. DE-AC02-06CH11357. We also acknowledge CDAC-UIC for helping with the laser drilling of gaskets.

Author contributions: SY and FL performed experiments. SY collected and analyzed the data. VIL conceived the study, supervised the project, and analyzed the results. KKP and JS assisted with experiments. SY and VIL prepared the manuscript.

Competing interests

The authors declare no competing interests.

Data availability

The data supporting this study's findings are available from the corresponding authors upon request.

Appendix

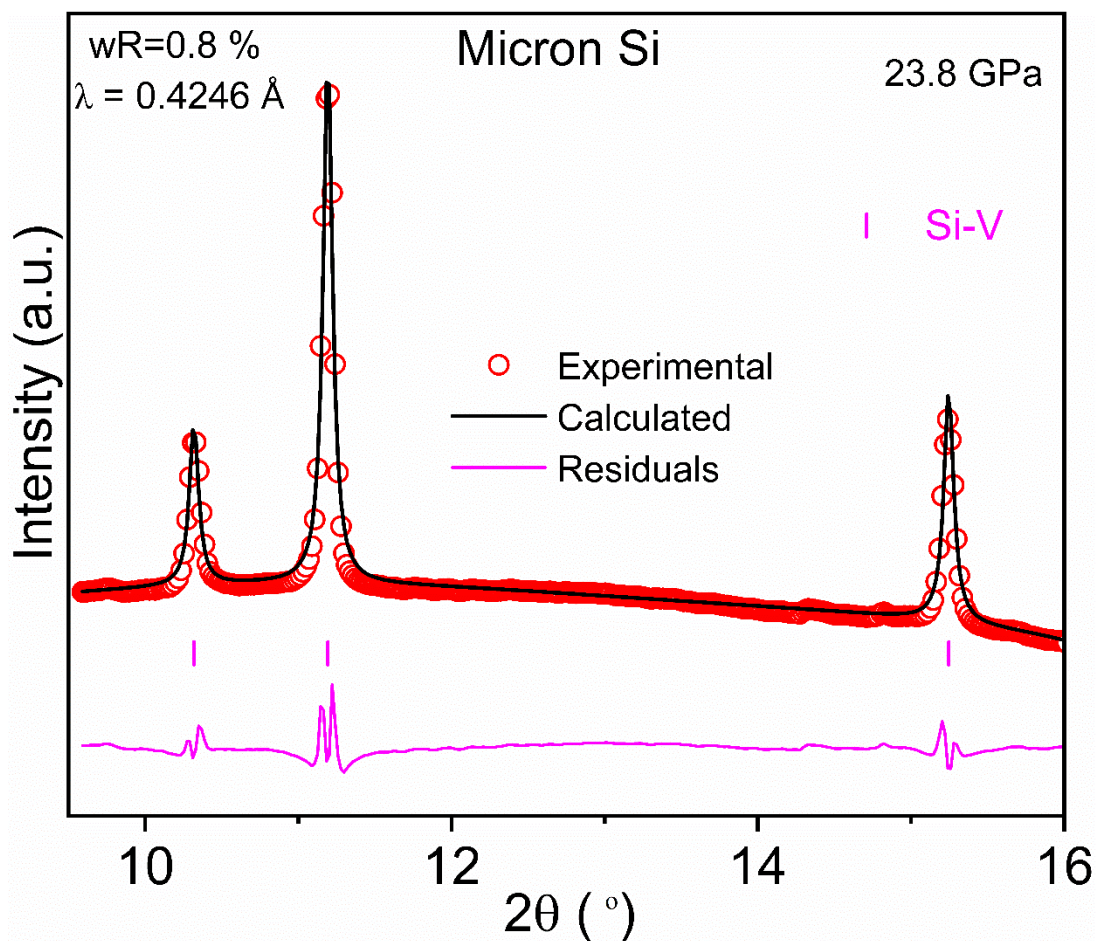


Fig. A1. Rietveld refinement of Si-V phase of micron Si at 23.8 GPa.

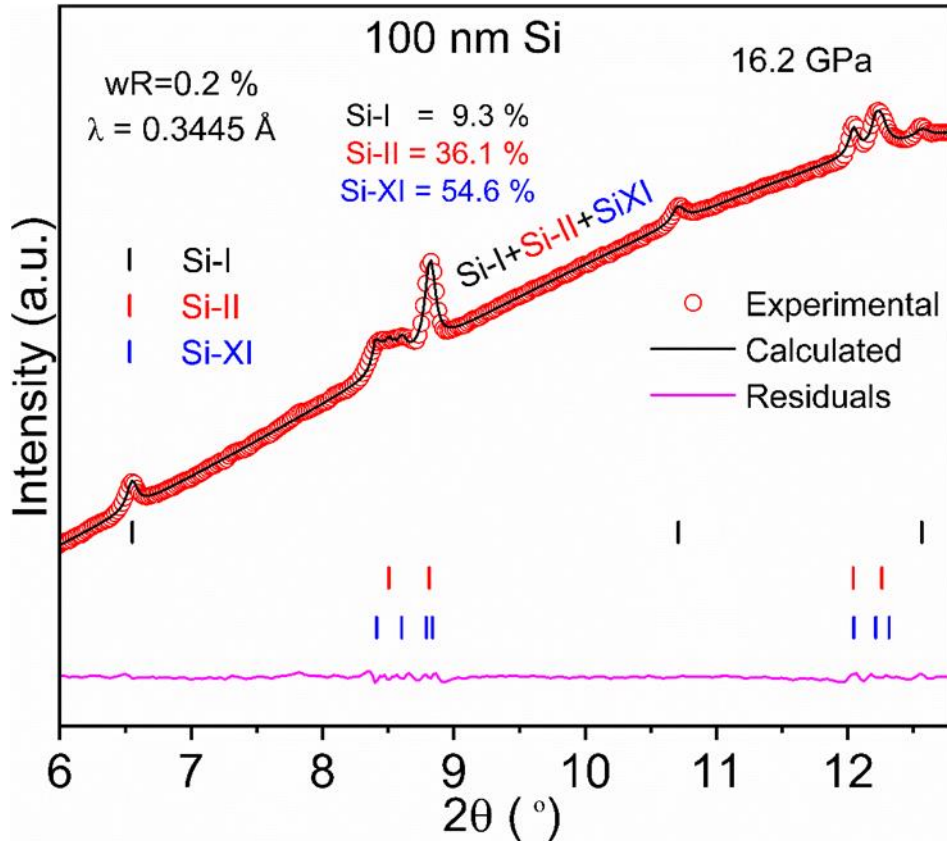


Fig. A2. Rietveld refinement of XRD patterns of 100 nm Si at 16.2 GPa. The Si-I, Si-II and Si-XI phases are coexisting. The phase fractions of all the phases are provided.

References

1. Craighead, H. G. Nanoelectromechanical systems. *Science* **290**, 1532-1535 (2000).
2. Rödl, C., Sander, T., Bechstedt, F., Vidal, J., Olsson, P., Laribi, S. & Gillemoles J.-F. Wurtzite silicon as a potential absorber in photovoltaics: Tailoring the optical absorption by applying strain. *Physical Review B* **92**, 045207 (2015).
3. Wippermann, S., He, Y., Vörös, M. & Galli, G. Novel silicon phases and nanostructures for solar energy conversion. *Applied Physics Reviews* **3**, 040807 (2016).
4. Cho, C.-H., Aspetti, C. O., Park, J. & Agarwal, R. Silicon coupled with plasmon nanocavities generates bright visible hot luminescence. *Nature Photonics* **7**, 285-289 (2013).
5. Owain Vaughan, A platform for quantum computing. *Nature Electronics* **6**, 337 (2023).
6. Haidong Zhang, Hanyu Liu, Kaya Wei, Oleksandr O. Kurakevych, Yann Le Godec, Zhenxian Liu, Joshua Martin, Michael Guerrette, George S. Nolas, and Timothy A. Strobel, BC8 Silicon (Si-III) is a Narrow-Gap Semiconductor. *Phys. Rev. Lett.* **118** 146601 (2017)
7. Hannelore Katzke, Ulrich Bismayer, and Pierre Tolédano, Theory of the high-pressure structural phase transitions in Si, Ge, Sn, and Pb. *Phys. Rev. B* **73**, 134105 (2006).

8. Hu, J. Z., Merkle, L. D., Menoni, C. S. & Spain, I. L. Crystal data for high-pressure phases of silicon. *Phys. Rev. B* **34**, 4679 (1986).
9. McMahon, M., Nelmes, R., Wright, N. & Allan, D. Pressure dependence of the Imma phase of silicon. *Physical Review B* **50**, 739 (1994).
10. Hwang, G. C., Blom, D. A., Vogt, T., Lee, J., Choi, H-J., Shao, S., Ma, Y. & Lee. Y. Pressure-driven phase transitions and reduction of dimensionality in 2D silicon nanosheets. *Nature Communications* **9**, 5412 (2018).
11. Lewis, S. P. & Cohen, M. L. Theoretical study of high-pressure orthorhombic silicon. *Phys. Rev. B* **48** 16144-16147 (1993).
12. Zarkevich, N. A., Chen, H., Levitas, V. I. & Johnson, D. D. Lattice instability during solid-solid structural transformations under a general applied stress tensor: Example of Si I→ Si II with metallization. *Physical Review Letters* **121**, 165701 (2018).
13. Zeng, Z. Q., Ge, M., Chen, B., Lou, H., Chen, X., Yan, J., Yang, W., Mao, H.-K., Yang, D., & Mao. W. L. Origin of plasticity in nanostructured silicon. *Physical Review Letters* **124**, 185701 (2020).
14. Wang, Y., Zhang, J., Wu, J., Coffey, J. L., Lin, Z., Sinogeikin, S. V., Yang, W. & Zhao, Y. Phase Transition and Compressibility in Silicon Nanowires. *Nano Letters* **8**, 2891-2895 (2008).
15. Huston, L. Q., Lugstein, A., Williams, J. S. & Bradby, J. E. The high pressure phase transformation behavior of silicon nanowires. *Applied Physics Letters* **113**, 123103 (2018).
16. Chrobak, D., Tymiak, N., Beaber, A., Ugurlu, O., Gerberich, W. W. & Nowak, R. Deconfinement leads to changes in the nanoscale plasticity of silicon. *Nature Nanotechnology* **6**, 480-484 (2011).
17. Zhao, Y., Buehler, F., Sites, J. & Spain, I. New metastable phases of silicon. *Solid State Commun.* **59**, 679 (1986).
18. J. Crain, G. J. Ackland, J. R. Maclean, R. O. Piltz, P. D. Hatton, and G. S. Pawley, Reversible pressure-induced structural transitions between metastable phases of silicon. *Phys. Rev. B* **50** 13043 (1994).
19. Piltz, R. O., Maclean, J. R., Clark, S. J., Ackland, G. J., Hatton, P. D. & Crain, J. Structure and properties of silicon XII: A complex tetrahedrally bonded phase. *Phys. Rev. B* **52**, 4072-4085 (1995).
20. Yesudhas, S., Levitas, V. I., Lin, F., Pandey, K. K. & Smith, J. Plastic strain-induced phase transformations in silicon: drastic reduction of transformation pressures, change in transformation sequence, and particle size effect. [[arXiv:2303.04407v1](https://arxiv.org/abs/2303.04407v1)].
21. Levitas, V. I. High-pressure mechanochemistry: conceptual multiscale theory and interpretation of experiments. *Physical Review B* **70**, 184118 (2004).
22. Levitas, V. I. High-pressure phase transformations under severe plastic deformation by torsion in rotational anvils. *Materials Transactions* **60**, 1294-1301 (2019).
23. Levitas V. I. Recent in situ Experimental and Theoretical Advances in Severe Plastic Deformations, Strain-Induced Phase Transformations, and Microstructure Evolution under High Pressure. *Material Transactions* **64**, 1866-1878 (2023).
24. Hemley, R. J., Mao, H. K., Shen, G., Badro, J., Gillet, P., Hanfland, M. & Hausermann, D. X-Ray imaging of stress and strain of Diamond, Iron, and Tungsten at megabar pressures. *Science* **276**, 1242-1245 (1997).

25. Li, B., Ji, C., Yang, W., Wang, J., Yang, K., Xu, R., Liu, W., Cai, Z., Chen, J. & Mao, H. K. Diamond anvil cell behavior up to 4 Mbar, *Proceedings of the National Academy of Sciences of the United States of America* **115**, 1713-1717 (2018).
26. Pandey, K. K. & Levitas, V. I. In situ quantitative study of plastic strain-induced phase transformations under high pressure: Example for ultra-pure Zr. *Acta Materialia*, **196**, 338-346 (2020).
27. Lin, F., Levitas V. I., Pandey K. K., Yesudhas S., and Park, C. In-situ study of rules of nanostructure evolution, severe plastic deformations, and friction under high pressure. *Materials Research Letters*, 2023, 11, 757-763.
28. Anzellini, S., Wharmby, M. T., Miozzi, F., Kleppe, A., Daisenberger, D. & Wilhelm, H. Quasi-hydrostatic equation of state of silicon up to 1 megabar at ambient temperature. *Scientific Reports* **9**, 15537 (2019).
29. Xuan, Y., Tan, L., Cheng, B., Zhang, F., Chen, X., Ge, M., Zeng, Q. & Zeng, Z. Pressure-induced phase transitions in nanostructured silicon. *The Journal of Physical Chemistry C* **124**, 27089-27096 (2020).
30. Levitas V. I. High pressure phase transformations revisited. Invited Viewpoint article. *Journal of Physics: Condensed Matter* **30**, 163001 (2018).
31. Klotz, S., Chervin, J., Munsch, P. & Marchand, G. L. Hydrostatic limits of 11 pressure transmitting media. *Journal of Physics D: Applied Physics* **42**, 075413 (2009).
32. Mao, H.-K. & Bell, P. M. High-pressure physics: the 1-megabar mark on the ruby R1 static pressure scale. *Science* **191**, 851-852 (1976).
33. Prescher, C. & Prakapenka V. B. DIOPTAS: a program for reduction of two-dimensional X-ray diffraction data and data exploration. *High Pressure Research* **35**, 223-230 (2015).
34. Toby, B. H. & Von Dreele, R. B. GSAS-II: the genesis of a modern open-source all purpose crystallography software package. *Journal of Applied Crystallography* **46**, 544-549 (2013)
35. Gonzalez-Platas, J., Alvaro, M., Nestola, F. & Angel, R. EosFit7-GUI: a new graphical user interface for equation of state calculations, analyses and teaching. *J. Appl. Cryst.* **49**, 1377–1382 (2016).
36. Shen, G., Ikuta, D., Sinogeikin, S., Li, Q., Zhang, Y. & Chen, C. Direct observation of a pressure-induced precursor lattice in silicon. *Physical Review Letters* **109**, 205503 (2012).
37. Domnich, V., Ge, D. & Gogotsi, Y. *Indentation-induced phase transformations in semiconductors*, in *High-Pressure Surface Science and Engineering* 381-442 (CRC Press, 2019).
38. Huston, L. Q., Lugstein, A., Williams, J. S. & J. E. Bradby. The high pressure phase transformation behavior of silicon nanowires. *Appl. Phys. Lett.* **113**, 123103 (2018).
39. Birch, F. Finite Elastic Strain of Cubic Crystals. *Phys. Rev.* **71**, 809–824 (1947).
40. Vinet, P., Ferrante, J., Rose, J. & Smith, J. Compressibility of solids. *J. Geophys. Res.* **92**, 9319 (1987).
41. McSkimin, H. & Andreatch, P. Elastic moduli of silicon vs hydrostatic pressure at 25.0 c and -195.8 c. *J. Appl. Phys.* **35**, 2161 (1964).
42. Qiu, S. L. & Marcu, P. M. Imma phase of Si: phase transitions and stability. *Eur. Phys. J. B* **81**, 411–418 (2011).